



Non-Hermitian bulk–boundary correspondence in quantum dynamics

Lei Xiao^{1,5}, Tianshu Deng^{2,5}, Kunkun Wang¹, Gaoyan Zhu¹, Zhong Wang³ , Wei Yi^{2,4} and Peng Xue¹

Bulk–boundary correspondence, a guiding principle in topological matter, relates robust edge states to bulk topological invariants. Its validity, however, has so far been established only in closed systems. Recent theoretical studies indicate that this principle requires fundamental revisions for a wide range of open systems with effective non-Hermitian Hamiltonians. Therein, the intriguing localization of nominal bulk states at boundaries, known as the non-Hermitian skin effect, suggests a non-Bloch band theory in which non-Bloch topological invariants are defined in generalized Brillouin zones, leading to a general bulk–boundary correspondence beyond the conventional framework. Here, we experimentally observe this fundamental non-Hermitian bulk–boundary correspondence in discrete-time non-unitary quantum-walk dynamics of single photons. We demonstrate pronounced photon localizations near boundaries even in the absence of topological edge states, thus confirming the non-Hermitian skin effect. Facilitated by our experimental scheme of edge-state reconstruction, we directly measure topological edge states, which are in excellent agreement with the non-Bloch topological invariants. Our work unequivocally establishes the non-Hermitian bulk–boundary correspondence as a general principle underlying non-Hermitian topological systems and paves the way for a complete understanding of topological matter in open systems.

Topological phases exhibit remarkable properties due to the presence of robust edge states at boundaries. These topologically protected edge states are related to bulk topological invariants through the principle of bulk–boundary correspondence, which is fundamentally important in topological matter^{1,2}. Intriguingly, recent theoretical studies have shown that the widely held bulk–boundary correspondence apparently breaks down in broad classes of non-Hermitian topological systems^{3–13}, where the bulk eigenstates of Hamiltonians are generically localized near boundaries by the non-Hermitian skin effect^{4,6,14}. To correctly account for topological edge states therein, an essential generalization of the conventional bulk–boundary correspondence must be introduced, where the non-Bloch-wave character of bulk states necessitates a new formulation of bulk topological invariants. With rapid progress in the experimental implementation of non-Hermiticity in synthetic systems ranging from photonics^{15–27} and phononics²⁸ to vacancy centres in solids²⁹ and cold atoms³⁰, non-Hermitian topological systems have recently generated intense interest^{31–39}. In particular, the fundamental issue of bulk–boundary correspondence and the underlying non-Hermitian skin effect have been under active theoretical investigations.

Here, we theoretically characterize and experimentally demonstrate the non-Hermitian skin effect and non-Hermitian bulk–boundary correspondence in discrete-time non-unitary quantum walks of single photons. We implement a non-unitary Floquet operator with polarization-dependent photon loss that supports Floquet topological phases protected by chiral symmetry. Using a domain-wall configuration, we demonstrate the non-Hermitian skin effect by observing that the walker becomes dynamically localized at the boundary with the onset of non-Hermiticity, regardless of its initial state and even in the absence of topological edge states. To demonstrate the non-Hermitian

bulk–boundary correspondence, we calculate the non-Bloch topological invariants defined in a generalized Brillouin zone⁴, taking into account the generic deviations of localized bulk states from extended Bloch waves. For our non-unitary quantum walks, two distinct topological invariants exist, corresponding to edge states with quasi-energies $\varepsilon=0$ and $\varepsilon=\pi$, respectively^{40,41}. As both topological edge states and bulk states are localized, it is challenging to unambiguously demonstrate the presence of edge states by following the common practice of measuring localized photon population. To overcome this difficulty, we devise a detection scheme involving quantum-state reconstruction at each time step, which allows us to differentiate edge states from bulk states and fully resolve the quasi-energy and the internal degrees of freedom of topological edge states. The experimentally measured topological edge states agree extremely well with the non-Bloch topological invariants of non-Bloch band theory^{4,7} and are robust against symmetry-preserving perturbations. Our experiment establishes the phenomenon of the non-Hermitian skin effect and associated non-Hermitian topology in the quantum regime, which not only enriches the scope of quantum simulation with photonics, but also paves the way for novel topological photonic devices based on non-Hermiticity.

Results

Chiral-symmetric non-unitary quantum walk. We focus on a chiral-symmetric non-unitary quantum walk on a one-dimensional lattice governed by the Floquet operator

$$U = R\left(\frac{\theta_1}{2}\right)S_2R\left(\frac{\theta_2}{2}\right)MR\left(\frac{\theta_2}{2}\right)S_1R\left(\frac{\theta_1}{2}\right), \quad (1)$$

in which the coin operator $R(\theta)$ rotates coin states by θ about the y axis, $R(\theta) = \mathbb{1}_w \otimes e^{-i\theta\sigma_y}$, where $\mathbb{1}_w = \sum_x |x\rangle\langle x|$ is the identity

¹Beijing Computational Science Research Center, Beijing, China. ²CAS Key Laboratory of Quantum Information, University of Science and Technology of China, Hefei, China. ³Institute for Advanced Study, Tsinghua University, Beijing, China. ⁴CAS Center for Excellence in Quantum Information and Quantum Physics, Hefei, China. ⁵These authors contributed equally: Lei Xiao, Tianshu Deng. ✉e-mail: wangzhongemail@tsinghua.edu.cn; wiyiz@ustc.edu.cn; gnepeux@gmail.com

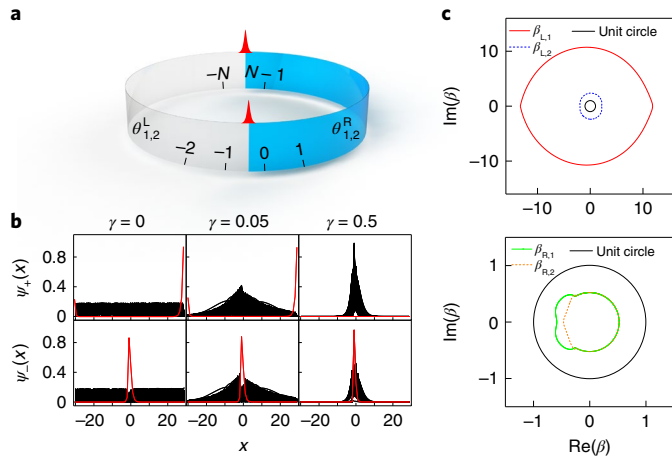


Fig. 1 | Quantum walks with the non-Hermitian skin effect. **a**, Schematic illustration of the domain-wall configuration. The lattice sites are labelled in a cyclic fashion, with the two boundaries located near $x=0$ and $x=-N$ (or $x=N-1$). The red peaks denote localized edge states at boundaries. **b**, Spatial distribution of the projected norms of bulk (black) and edge (red) states with various γ values and $\psi_{\pm}(x) = |(\langle x| \otimes \langle \pm |)|\psi\rangle|$. Here, $|\pm\rangle = (|0\rangle \pm |1\rangle)/\sqrt{2}$ are eigenstates of the chiral-symmetry operator, and $|\psi\rangle$ is defined in equation (2). **c**, Generalized Brillouin zones parametrized by the spatial-mode functions $\beta_{a,j}$ for $\gamma=0.5$. Whereas the standard Brillouin zones are indicated by unit circles (solid black line), two distinct generalized Brillouin zones exist for each given bulk. Parameters for the numerical calculations in **b** and **c** are $N=30$, $\theta_1^R = 0.1875\pi$, $\theta_1^L = -0.3333\pi$, $\theta_2^R = 0.2\pi$ and $\theta_2^L = -0.6667\pi$.

operator in lattice space, with x being the site index and the subscript (w) standing for walker. Here, i is the square root of -1 and σ_y is a Pauli matrix. The shift operator S_1 (S_2) shifts the walker in the coin state $|1\rangle$ ($|0\rangle$), the eigenstate of the Pauli matrix σ_z with eigenvalue -1 ($+1$), to the right (left) by one lattice site: $S_1 = \sum_x |x\rangle\langle x| \otimes |0\rangle\langle 0| + |x+1\rangle\langle x| \otimes |1\rangle\langle 1|$, $S_2 = \sum_x |x-1\rangle\langle x| \otimes |0\rangle\langle 0| + |x\rangle\langle x| \otimes |1\rangle\langle 1|$. Non-unitarity is introduced through the gain/loss operator $M = \mathbb{1}_w \otimes (e^\gamma |0\rangle\langle 0| + e^{-\gamma} |1\rangle\langle 1|)$, where γ is a tuneable gain/loss parameter. Quantum-walk dynamics is periodically driven by U , with the time-evolved state $|\Phi(t)\rangle = U^t |\Phi(0)\rangle$ at time step t ($t=0,1,2,\dots$). It follows that a quantum walk stroboscopically simulates the non-unitary time evolution driven by a non-Hermitian effective Hamiltonian H_{eff} , with $U := e^{-iH_{\text{eff}}}$. Whereas key properties of U are reflected in the eigenstates and eigenspectrum (known as the quasi-energy spectrum) of H_{eff} , the explicit form of H_{eff} is cumbersome in our case (see Supplementary Information). We therefore mainly focus on the characterization of U itself.

A key property of U is its chiral symmetry: $\sigma_x U \sigma_x = U^{-1}$ (where σ_x is the standard Pauli matrix), which can be cast into the more familiar form $\sigma_x H_{\text{eff}} \sigma_x = -H_{\text{eff}}$ (note that the chiral symmetry here is referred to as the sublattice symmetry in ref. ³⁵). Importantly, when the lattice has boundaries, U exhibits the non-Hermitian skin effect, in which all of its eigenstates become localized near the boundaries. The non-Hermitian skin effect of U distinguishes it from previous experimentally realized non-unitary quantum walks^{15–21}.

To investigate the non-Hermitian skin effect and non-Hermitian bulk–boundary correspondence of U , we consider a domain-wall configuration on a circle, as shown in Fig. 1a, where the left and right bulks have different coin parameters, denoted $\theta_{1(2)}^L$ and $\theta_{1(2)}^R$, respectively. The lattice sites are indexed in a cyclic fashion, with $x \in J_L$ (where $J_L = \{x \in \mathbb{Z} | -N \leq x \leq -1\}$ and \mathbb{Z}

stands for the set of integers) for the left bulk, and $x \in J_R$ (where $J_R = \{x \in \mathbb{Z} | 0 \leq x \leq N-1\}$) for the right.

In Fig. 1b, we numerically demonstrate that all the bulk eigenstates of U are localized at the boundaries for finite γ , a hallmark of the non-Hermitian skin effect. Except for a few critical values of parameters, the bulk quasi-energy spectrum of the system features a gap near $\varepsilon=0$ or $\varepsilon=\pi$, reflecting the Floquet nature of the system^{40,41}. This gap can be regarded as either a line gap or a point gap³⁵, since our theoretical characterization of the non-Bloch topological invariants works in either case. Two distinct types of topological edge state with $\varepsilon=0$, $\varepsilon=\pi$ can emerge within the corresponding band gap, with coin states $|\pm\rangle = (|0\rangle \pm |1\rangle)/\sqrt{2}$ as dictated by chiral symmetry.

Whereas the non-Hermitian skin effect can be intuitively understood through the reflection of bulk-state wave functions at boundaries¹⁴, quantitative insights into the phenomenon are obtained by focusing on the eigenequation $U|\psi\rangle = \lambda|\psi\rangle$ (λ is the eigenvalue of U), and writing the bulk-eigenstate wave functions as^{4,7,42}

$$|\psi\rangle = \sum_a \sum_{x \in J_{a,j}} \beta_{a,j}^x |x\rangle \otimes |\phi_j^a\rangle_c \quad (\alpha = L, R), \quad (2)$$

where $\beta_{L(R),j}$ is the spatial-mode function for the j th mode in the left (right) bulk, and $|\phi_j^{L(R)}\rangle_c$ is the corresponding coin state. For the domain-wall configuration considered here, two spatial modes (labelled by $j=1,2$) exist for each bulk (see Supplementary Information). In the unitary limit with $\gamma=0$, $|\beta_{a,1}| = |\beta_{a,2}| = 1$, and we identify $\beta_{a,j}$ as e^{ik} , with k the quasi-momentum in the first Brillouin zone and $|\psi\rangle$ reduced to the Bloch wave functions. For a finite γ and with the domain-wall configuration, however, $|\beta_{a,j}| \neq 1$, which underlies the non-Hermitian skin effect.

According to topological band theory, the topological invariants of U are^{43,44}

$$\nu_\varepsilon = \frac{1}{4\pi i} \int_0^{2\pi} \text{Tr} \left[\sigma_x (\overline{U}_\varepsilon(k))^{-1} d(\overline{U}_\varepsilon(k)) \right] \quad (\varepsilon = 0, \pi), \quad (3)$$

where $\overline{U}_\varepsilon(k)$ is the periodized Floquet operator in quasi-momentum k space associated with the non-Hermitian effective Hamiltonian $H_{\text{eff}}^\varepsilon = i \ln_\varepsilon U$, with the subscript ε in \ln_ε indicating a branch cut at ε (see Methods). Correspondingly, ν_0, ν_π dictates a topological edge state with $\varepsilon=0$ ($\varepsilon=\pi$).

For our domain-wall system with the non-Hermitian skin effect, however, these Bloch topological invariants cannot correctly predict topological edge states. The exponential localization of the nominal bulk states at the domain wall suggests that the conventional Brillouin zone with real-valued k should not be the appropriate starting point. Instead, since the Bloch phase factor e^{ik} is replaced by $\beta_{a,j} := |\beta_{a,j}(p_j^\alpha)| e^{ip_j^\alpha}$, we need to use the generalized Brillouin zone⁴, parametrized by the phase parameter p_j^α . As p_j^α varies, the allowed values of $\beta_{a,j}$ form one-dimensional trajectories in the complex plane, with the bulk quasi-energy spectrum of the system given by eigenvalues of $H_{\text{eff}}(e^{ik} \rightarrow \beta_{a,j})$. Thus, these trajectories (illustrated in Fig. 1c) fundamentally generalize the concept of Brillouin zones in one-dimensional Hermitian systems to generic one-dimensional non-Hermitian settings and are referred to as the generalized Brillouin zones. The non-Bloch topological invariants $\tilde{\nu}_0, \tilde{\nu}_\pi$ are defined over these generalized Brillouin zones (see Methods).

As shown in Fig. 1c, two distinct generalized Brillouin zones can be found for a single bulk, corresponding to the two distinct spatial modes $j=1$ and $j=2$, respectively. However, we have numerically checked that equation (3) yields the same set of $\tilde{\nu}_0, \tilde{\nu}_\pi$ when integrated over different generalized Brillouin zones of the same bulk (see Supplementary Information). As we experimentally demonstrate in the following, these non-Bloch topological invariants correctly predict the existence of both types of topological edge state

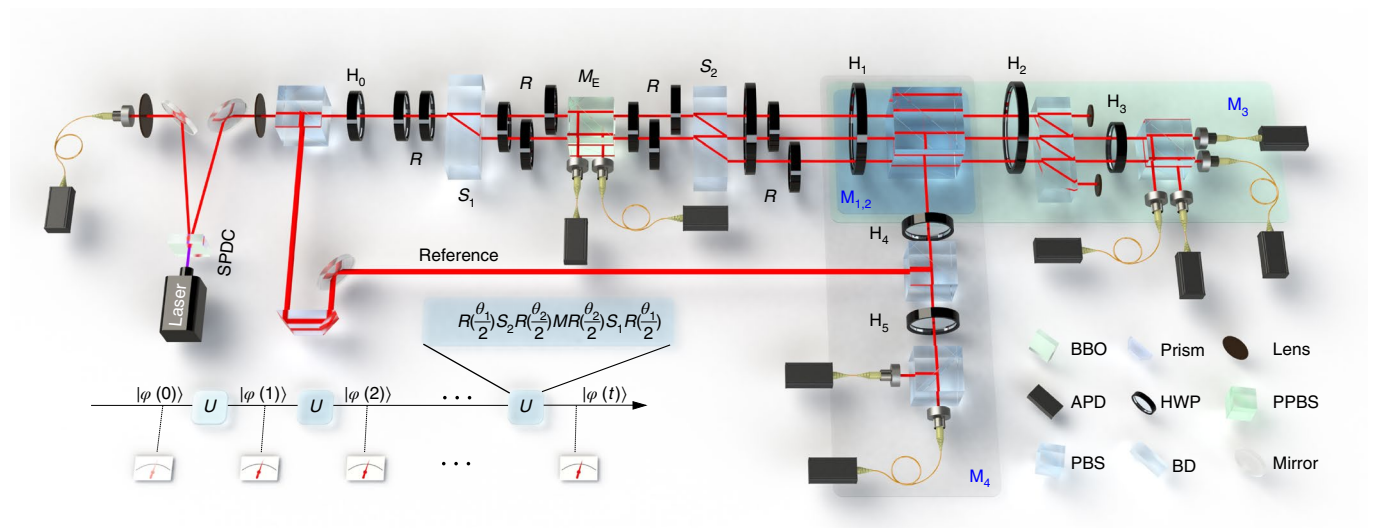


Fig. 2 | Experimental implementation. A pair of photons is created via spontaneous parametric down-conversion (SPDC) using a β -barium-borate (BBO) non-linear crystal pumped by a diode laser. One of the photons serves as the trigger, while the other (the walker photon) is projected onto one of the polarization states via a polarizing beam splitter (PBS) and a half-wave plate (HWP) labelled 'H₀'. It then proceeds through an interferometric network composed of HWPs (H₀–H₅), beam displacers (BD) and partially polarizing beam splitters (PPBS). For each detection module M_i ($i = 1, 2, 3, 4$), the walker photon is detected by avalanche photodiodes (APD), in coincidence with the trigger photon. A reference photon is also used for edge-state detection (see Methods). As an illustration, we show the set-up for the first step of the quantum-walk configuration and a conceptual representation of the multiple-step quantum-walk dynamics (lower left corner). Note that the detection modules are attached to only the last step of the quantum-walk configuration, as we sequentially increase the number of steps to probe the dynamics of the walker photon.

with $\varepsilon = 0$, $\varepsilon = \pi$, which unambiguously embodies the non-Hermitian bulk–boundary correspondence.

Experimental demonstration of the non-Hermitian skin effect.

We experimentally investigate non-unitary quantum-walk dynamics governed by U using a single-photon interferometer set-up, as illustrated in Fig. 2. The coin states are encoded in the photon polarizations, with $|0\rangle$ and $|1\rangle$ corresponding to the horizontally and vertically polarized photons, respectively. The walker states are encoded in the spatial mode of the photons. We experimentally realize a mode-selective loss operator $M_E = \mathbb{1}_w \otimes (|0\rangle\langle 0| + \sqrt{1-p}|1\rangle\langle 1|)$, which enforces a partial measurement in the basis of $\{|0\rangle, |1\rangle\}$ at every time step. Since $M = e^\gamma M_E$ with $\gamma = -\frac{1}{4} \ln(1-p)$, it is straightforward to map the experimentally implemented dynamics to those with U by multiplying a time-dependent factor $e^{\gamma t}$.

We first demonstrate the non-Hermitian skin effect through the local accumulation of population at long times in the absence of topological edge states. We study seven-step quantum-walk dynamics and focus on a single boundary in the domain-wall configuration. Initializing the walker at $x = -1$, but with different coin states, we first implement unitary quantum walks with $\gamma = 0$. As illustrated in Fig. 3a–d, the spatial photon distribution becomes increasingly non-local in time. In contrast, when choosing a finite γ (Fig. 3e–h), the population distribution after seven steps is still localized near the boundary, regardless of the initial coin state. Crucially, for both the unitary and non-unitary cases, we choose the coin parameters such that no topological edge states exist, which is numerically confirmed by the absence of 0 or π modes in the quasi-energy spectra. The localization of the population distribution is therefore the unequivocal manifestation of the localization of bulk eigenstates by the non-Hermitian skin effect.

Non-Hermitian bulk–boundary correspondence. We now proceed to a systematic study of non-Hermitian bulk–boundary correspondence, or non-Bloch bulk–boundary correspondence, by matching the presence of 0 and π modes with non-Bloch topological

invariants. However, it is challenging to differentiate topological edge states from bulk states by measuring probability distribution, as both states are localized at the boundary due to the non-Hermitian skin effect.

To overcome this difficulty, we develop a detection scheme that allows us to extract edge-state wave functions with spatial and coin-state resolution. Formally, writing the time-evolved wave function as $|\Phi(t)\rangle$ (see Methods), we construct the time-integrated wave functions

$$|\Phi_\varepsilon(t)\rangle = \sum_{t'=0}^t \frac{e^{i\varepsilon t'}}{t+1} |\Phi(t')\rangle \quad (\varepsilon = 0, \pi). \quad (4)$$

As we show in Methods, in the weighted summation of equation (4), time-dependent phases of bulk states cancel out at long times, provided that the quasi-energy spectrum underlying the dynamics is purely real. The resulting $|\Phi_\varepsilon(t)\rangle$ would converge to the corresponding edge-state wave function with ε at sufficiently large time steps, given that the initial state has a finite overlap with the corresponding edge state. Due to chiral symmetry, topological edge states are necessarily in the coin state $|\pm\rangle$, which are eigenstates of the symmetry operator. Projecting the integrated wave function from equation (4) onto the chiral-symmetry basis $|\pm\rangle$, we measure the quantity (see Methods for details)

$$\Phi_{\varepsilon,\mu}(x) = |(\langle x| \otimes \langle \mu|) |\Phi_\varepsilon(t)\rangle| \quad (\mu = \pm), \quad (5)$$

which, as we show in the following, converges to the norm of the corresponding edge-state wave function (apart from a global scaling factor) after seven steps of a quantum walk. The existence and properties (ε and coin state $|\mu\rangle$) of topological edge states are directly reflected as prominent peaks in the corresponding $\Phi_{\varepsilon,\mu}(x)$ from the experimental measurement. Since a prerequisite for our detection scheme is the presence of a purely real energy spectrum, for the following experiments, we choose the coin parameters for which the

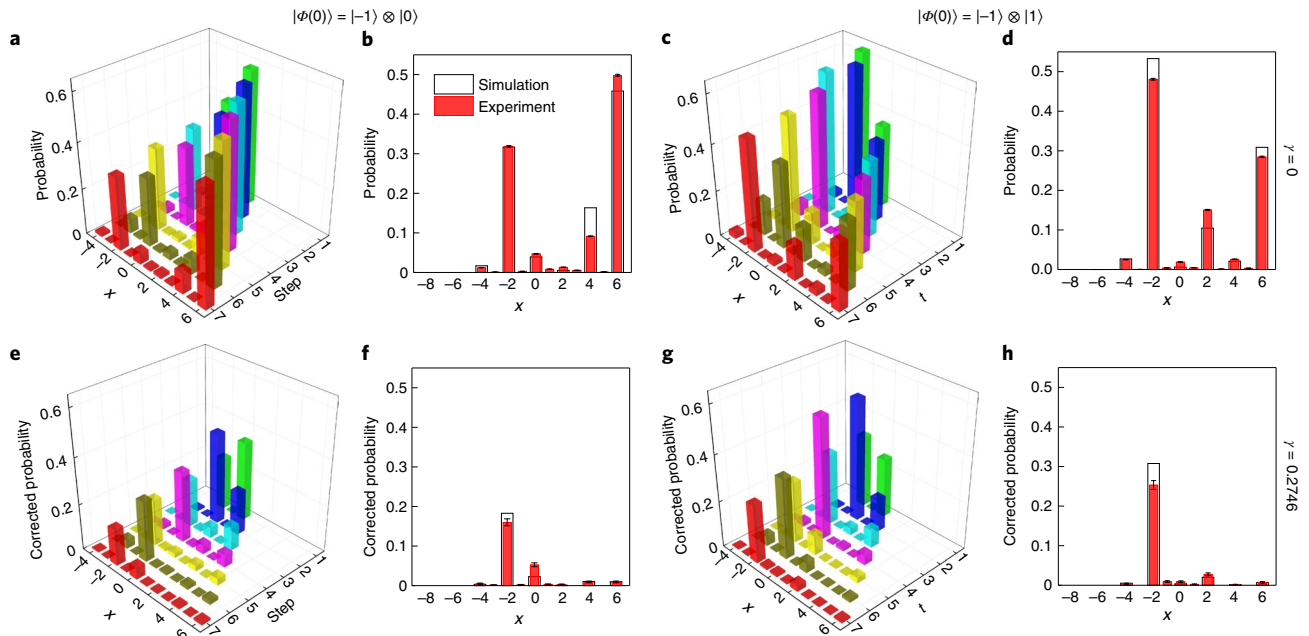


Fig. 3 | Experimental demonstration of the non-Hermitian skin effect. **a–d**, Spatial probability distributions of a seven-step unitary quantum walk with $\gamma=0$ and different initial states $|\Phi(0)\rangle$. **a, c**, The time-dependent probability distributions with the initial states $|\Phi(0)\rangle = |-1\rangle \otimes |0\rangle$ and $|\Phi(0)\rangle = |-1\rangle \otimes |1\rangle$, respectively. **b, d**, The distributions at the last time step for the two initial states, respectively. **e–h**, Spatial probability distributions of a seven-step non-unitary quantum walk with $\gamma=0.2746$ and different initial states $|\Phi(0)\rangle$. **e, g**, The time-dependent probability distributions with the initial states $|\Phi(0)\rangle = |-1\rangle \otimes |0\rangle$ and $|\Phi(0)\rangle = |-1\rangle \otimes |1\rangle$, respectively. **f, h**, The distributions at the last step with these initial states, respectively. The coin parameters are $\theta_1^R = 0.0667\pi$, $\theta_1^I = 0.5625\pi$, $\theta_2^R = 0$ and $\theta_2^I = \pi$, where no topological edge states exist for either $\gamma=0$ or $\gamma=0.2746$. For the coloured bars in **a, c, e, g**, different colours correspond to different time steps. Error bars represent standard deviations due to photon-counting statistics, where $\sim 10^5$ photons are used for each measurement.

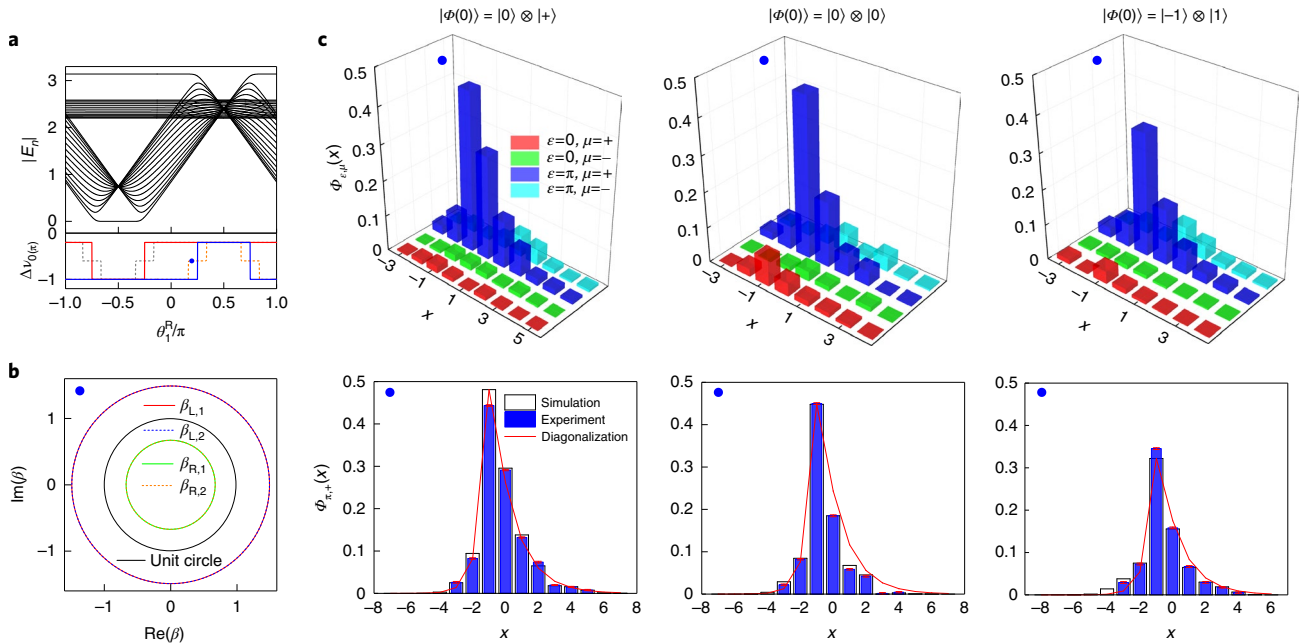


Fig. 4 | Non-Bloch bulk-boundary correspondence for edge states with $\epsilon = \pi$. **a**, Quasi-energy spectrum E_n (black), and winding-number differences for 0 (red) and π (blue) modes. Here, E_n is defined through $\lambda = e^{-iE_n}$ (see Methods). The non-Bloch winding numbers (solid) are different from the Bloch ones (dashed; grey (orange) for $\epsilon=0$ ($\epsilon=\pi$)). The blue dot indicates the parameter for **c, b**. **b**, Generalized Brillouin zones characterized by β_{α} on the complex plane. **c**, Upper row: experimentally measured $\Phi_{\pi,+}(x)$ after the seventh step with different initial states. Lower row: comparison of experimentally measured and numerically simulated $\Phi_{\pi,+}(x)$. We also show the scaled norms of the edge state with $\epsilon=\pi$ after the seventh step, calculated by diagonalizing a domain-wall system with $N=15$. Norms of the edge states from diagonalization are scaled to fit the central peak of the numerically simulated $\Phi_{\pi,+}(x)$. For all panels, $\theta_1^I = 0.5625\pi$, $\theta_2^R = 0.25\pi$, $\theta_2^I = 0.75\pi$ and $\gamma=0.2746$. For **b** and **c**, $\theta_1^R = 0.18\pi$, the system supports only one topological edge state, consistent with measurements in **c**. Error bars represent standard deviations due to photon-counting statistics.

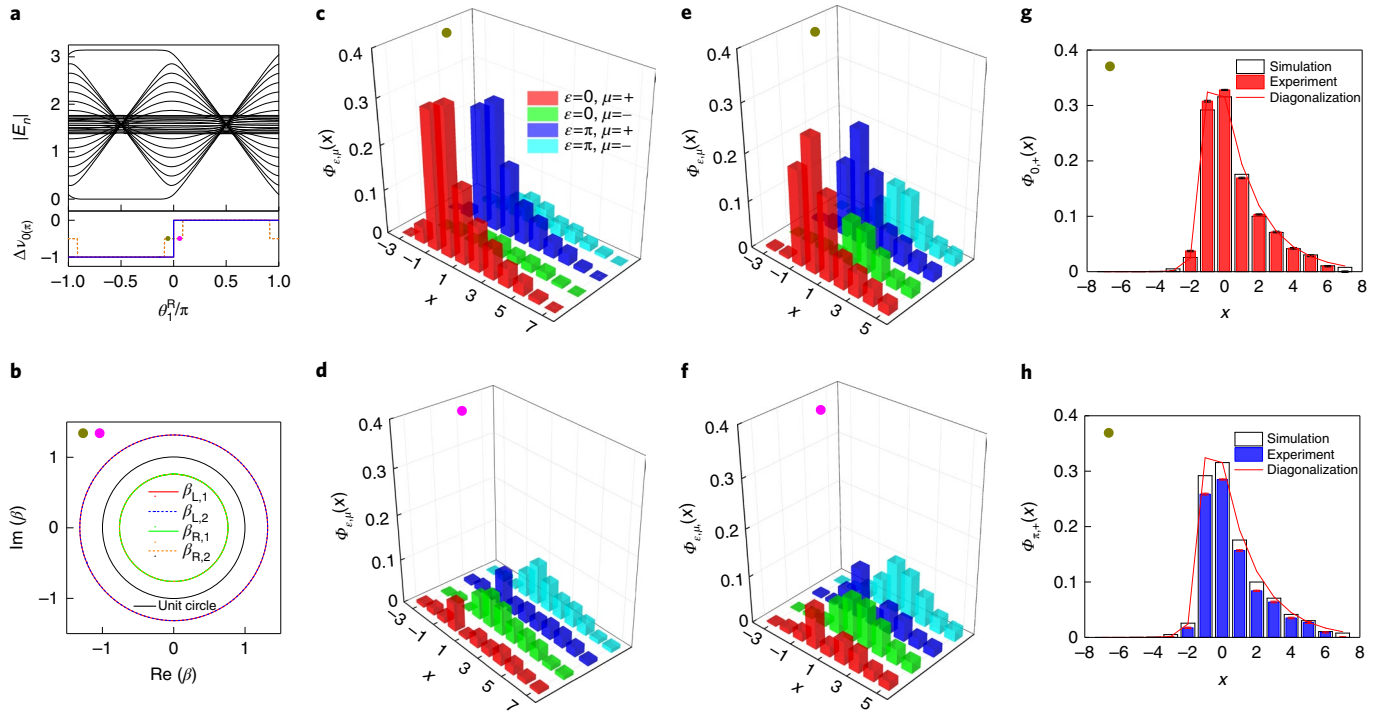


Fig. 5 | Evidence for non-Bloch bulk-boundary correspondence. **a**, Quasi-energy spectrum, and winding-number differences for 0 and π modes between the two bulks, with $\theta_1^R = 0.5625\pi$, $\theta_2^R = 0$, $\theta_2^R = \pi$ and $\gamma = 0.2746$. Colours and lines are the same as those in Fig. 4. Note that the two solid lines in the lower panel here overlap with each other, as do the two dashed lines. The green dot, with $\theta_1^R = -0.0667\pi$, corresponds to the parameter used in **c, e, g, h**, where two topological edge states exist, consistent with measurement in **c**. The magenta dot, with $\theta_1^R = 0.0667\pi$, corresponds to the parameter used in **d, f**, where no topological edge states exist, consistent with measurement in **d**. **b**, Generalized Brillouin zones on the complex plane. **c, d**, Experimentally measured $\Phi_{\varepsilon,\mu}(x)$ where both types of edge state exist (**c**) and no edge states exist (**d**) after the seventh step, with the initial state $|0\rangle \otimes |+\rangle$. **e, f**, Robustness of edge states against static disorder where both types of edge state exist (**e**) and no edge states exist (**f**). Measured $\Phi_{\varepsilon,\mu}(x)$ of a five-step quantum walk with disordered coin parameter $\theta_1^R + \delta\theta$, where $\delta\theta \in [-\pi/20, \pi/20]$ is fixed for each position, independent of time. **g, h**, Comparison of experimentally measured and numerically calculated $\Phi_{0,+}(x)$ (**g**) and $\Phi_{\pi,+}(x)$ (**h**), and the scaled norms of the corresponding edge state after the seventh step. Error bars represent standard deviations due to photon-counting statistics.

quasi-energy spectra of our domain-wall configuration are purely real. Interestingly, this is ensured by a boundary-induced parity-time symmetry¹⁵. We further note that the two types of band gap (line gap and point gap) become equivalent in the case of real quasi-energy spectra.

First, we choose the parameters such that a π -mode edge state exists in the numerically calculated quasi-energy spectrum (Fig. 4a). Note that the two generalized Brillouin zones in each bulk overlap in this case, as illustrated in Fig. 4b. We initialize the walker in three different initial states and let it evolve for seven steps before we measure $\Phi_{\varepsilon,\mu}(x)$. As shown in the upper row of Fig. 4c, regardless of initial states, a prominent peak exists only for the $\Phi_{\pi,+}(x)$ measurement, clearly indicating the presence of a π -mode edge state with the coin state $|+\rangle$. The finite, but much smaller, signals in $\Phi_{\pi,-}(x)$ or $\Phi_{0,\pm}(x)$ are due to systematic error of our detection scheme at finite steps.

In the lower row of Fig. 4c, we see that the measured $\Phi_{\pi,+}(x)$ at the seventh step agrees well with the result from numerical simulations for a seven-step quantum walk. Moreover, $\Phi_{\pi,+}(x)$ approaches the scaled norms of the edge-state wave function, calculated by diagonalizing a finite ($N=15$) domain-wall system with the same parameters. From Fig. 4a, we see that, for our chosen parameters, only the non-Bloch winding numbers, $(\Delta\tilde{\nu}_0, \Delta\tilde{\nu}_\pi) = (0, -1)$, correctly predict the presence of the π -mode edge state. Here, $\Delta\tilde{\nu}_{0(\pi)} = \tilde{\nu}_{0(\pi)}^L - \tilde{\nu}_{0(\pi)}^R$. For comparison, the corresponding Bloch winding numbers are $(\Delta\nu_0, \Delta\nu_\pi) = (0, -1/2)$.

We then perform a series of experiments with parameters where: (1) both $\varepsilon=0$ and $\varepsilon=\pi$ edge states exist; (2) no topological state exists. As shown in Fig. 5a, in both cases, the theoretically calculated non-Bloch topological invariants correctly predict the existence of topological edge states, whereas the Bloch topological invariants fail to do so. Specifically, in the case where both types of edge state exist (Fig. 5c), $(\Delta\tilde{\nu}_0, \Delta\tilde{\nu}_\pi) = (-1, -1)$, while $(\Delta\nu_0, \Delta\nu_\pi) = (-1/2, -1/2)$. In the case where there is no edge state (Fig. 5d), $(\Delta\tilde{\nu}_0, \Delta\tilde{\nu}_\pi) = (0, 0)$, while $(\Delta\nu_0, \Delta\nu_\pi) = (-1/2, -1/2)$. Note that the generalized Brillouin zones for the two cases in Fig. 5c,d are the same, as shown in Fig. 5b.

An important feature of topological edge states is their robustness to symmetry-preserving perturbation. As an experimental confirmation, we introduce static disorders to the coin rotations by modulating the setting angles of the corresponding half-wave plates (HWP) by a small random amount $\delta\theta \in [-\pi/20, \pi/20]$ around θ_1^R . Here, $\delta\theta$ is position dependent, but time independent. Such static disorders preserve the chiral symmetry of U . As shown in Fig. 5e, the measured $\Phi_{\varepsilon,\mu}(x)$ of a five-step quantum walk indicates the robustness of both types of edge state. In contrast, as illustrated in Fig. 5f, the same level of static disorder would not induce peaks in the measured $\Phi_{\varepsilon,\mu}(x)$ in the absence of topological edge states.

Finally, in Fig. 5g,h we show the measured $\Phi_{0,+}(x)$ and $\Phi_{\pi,+}(x)$ after the last time step, which agree well with results from numerical simulations and with scaled norms of the numerically calculated edge-state wave functions. Our results thus unambiguously confirm the non-Hermitian bulk-boundary correspondence.

Discussion

We have experimentally observed the non-Hermitian skin effect and non-Hermitian (non-Bloch) bulk–boundary correspondence in discrete-time non-unitary quantum-walk dynamics. Our theoretical approach can be extended to general non-unitary dynamics, which host rich topological phenomena beyond their unitary counterparts. Our experiment highlights the versatility of quantum-walk dynamics in studying non-Hermitian topological systems. Specifically, the detection scheme developed in this work allows us to differentiate topological edge states from bulk states localized by the non-Hermitian skin effect, which is valuable for the exploration of non-Hermitian topological systems in general. Besides its fundamental importance for understanding topological matter in generic open systems, our observation would directly stimulate further explorations of non-Hermitian topology with photonics. It would also inspire the designs of novel open-system-based devices, making use of the interplay between the non-Hermitian skin effect, parity–time symmetry and robust topological edge states. An outstanding example would be the design of novel topological lasing based on the non-Bloch topology observed here.

Note added in proof: Since completing this work, we have learned of related experiments in classical systems^{46,47}. Our experimental platform is quantum mechanical.

Online content

Any methods, additional references, Nature Research reporting summaries, source data, extended data, supplementary information, acknowledgements, peer review information; details of author contributions and competing interests; and statements of data and code availability are available at <https://doi.org/10.1038/s41567-020-0836-6>.

Received: 31 December 2019; Accepted: 11 February 2020;

Published online: 16 March 2020

References

- Hasan, M. Z. & Kane, C. L. Colloquium: topological insulators. *Rev. Mod. Phys.* **82**, 3045–3067 (2010).
- Qi, X. L. & Zhang, S. C. Topological insulators and superconductors. *Rev. Mod. Phys.* **83**, 1057–1110 (2011).
- Lee, T. E. Anomalous edge state in a non-Hermitian lattice. *Phys. Rev. Lett.* **116**, 133903 (2016).
- Yao, S. & Wang, Z. Edge states and topological invariants of non-Hermitian systems. *Phys. Rev. Lett.* **121**, 086803 (2018).
- Yao, S., Song, F. & Wang, Z. Non-Hermitian Chern bands. *Phys. Rev. Lett.* **121**, 136802 (2018).
- Kunst, F. K., Edvardsson, E., Budich, J. C. & Bergholtz, E. J. Biorthogonal bulk–boundary correspondence in non-Hermitian systems. *Phys. Rev. Lett.* **121**, 026808 (2018).
- Yokomizo, K. & Murakami, S. Non-Bloch band theory of non-Hermitian systems. *Phys. Rev. Lett.* **123**, 066404 (2019).
- Alvarez, V. M., Vargas, J. B., Berdakin, M. & Torres, L. F. Topological states of non-Hermitian systems. *Eur. Phys. J. Spec. Top.* **227**, 1295–1308 (2018).
- Lee, C. H. & Thoma, R. Anatomy of skin modes and topology in non-Hermitian systems. *Phys. Rev. B* **99**, 201103(R) (2019).
- Ghatak, A. & Das, T. New topological invariants in non-Hermitian systems. *J. Phys. Condens. Matter* **31**, 263001 (2019).
- Borgnia, D. S., Kruchkov, A. J. & Slager, R.-J. Non-Hermitian boundary modes. *Phys. Rev. Lett.* **124**, 056802 (2020).
- Martinez Alvarez, V. M., Barrios Vargas, J. E. & Foa Torres, L. E. F. Non-Hermitian robust edge states in one dimension: anomalous localization and eigenspace condensation at exceptional points. *Phys. Rev. B* **97**, 121401(R) (2018).
- Longhi, S. Probing non-Hermitian skin effect and non-Bloch phase transitions. *Phys. Rev. Res.* **1**, 023013 (2019).
- McDonald, A., Pereg-Barnea, T. & Clerk, A. A. Phase-dependent chiral transport and effective non-Hermitian dynamics in a bosonic Kitaev–Majorana chain. *Phys. Rev. X* **8**, 041031 (2018).
- Poli, C., Bellec, M., Kuhl, U., Mortessagne, F. & Schomerus, H. Selective enhancement of topologically induced interface states in a dielectric resonator chain. *Nat. Commun.* **6**, 6710 (2015).
- Zeuner, J. M. et al. Observation of a topological transition in the bulk of a non-Hermitian system. *Phys. Rev. Lett.* **115**, 040402 (2015).
- Xiao, L. et al. Observation of topological edge states in parity–time-symmetric quantum walks. *Nat. Phys.* **13**, 1117–1123 (2017).
- Zhan, X. et al. Detecting topological invariants in nonunitary discrete-time quantum walks. *Phys. Rev. Lett.* **119**, 130501 (2017).
- Xiao, L. et al. Higher winding number in a nonunitary photonic quantum walk. *Phys. Rev. A* **98**, 063847 (2018).
- Wang, K. et al. Simulating dynamic quantum phase transitions in photonic quantum walks. *Phys. Rev. Lett.* **122**, 020501 (2019).
- Wang, K. et al. Observation of emergent momentum–time skyrmions in parity–time-symmetric non-unitary quench dynamics. *Nat. Commun.* **10**, 2293 (2019).
- Xiao, L. et al. Observation of critical phenomena in parity–time-symmetric quantum dynamics. *Phys. Rev. Lett.* **123**, 230401 (2019).
- Weimann, S. et al. Topologically protected bound states in photonic parity–time-symmetric crystals. *Nat. Mater.* **16**, 433–438 (2017).
- Parto, M. et al. Edge-mode lasing in 1D topological active arrays. *Phys. Rev. Lett.* **120**, 113901 (2018).
- Zhou, H. et al. Observation of bulk Fermi arc and polarization half charge from paired exceptional points. *Science* **359**, 1009–1012 (2018).
- Ozawa, T. et al. Topological photonics. *Rev. Mod. Phys.* **91**, 015006 (2019).
- Bandres, M. A. et al. Topological insulator laser: experiments. *Science* **359**, eaar4005 (2018).
- Zhu, W. et al. Simultaneous observation of a topological edge state and exceptional point in an open and non-Hermitian acoustic system. *Phys. Rev. Lett.* **121**, 124501 (2018).
- Wu, Y. et al. Observation of parity–time symmetry breaking in a single-spin system. *Science* **364**, 878–880 (2019).
- Li, J. et al. Observation of parity–time symmetry breaking transitions in a dissipative Floquet system of ultracold atoms. *Nat. Commun.* **10**, 855 (2019).
- Shen, H., Zhen, B. & Fu, L. Topological band theory for non-Hermitian Hamiltonians. *Phys. Rev. Lett.* **120**, 146402 (2018).
- Leykam, D., Bliokh, K. Y., Huang, C., Chong, Y. D. & Nori, F. Edge modes, degeneracies, and topological numbers in non-Hermitian systems. *Phys. Rev. Lett.* **118**, 040401 (2017).
- Gong, Z. et al. Topological phases of non-Hermitian systems. *Phys. Rev. X* **8**, 031079 (2018).
- El-Ganainy, R. et al. Non-Hermitian physics and PT symmetry. *Nat. Phys.* **14**, 11–19 (2018).
- Kawabata, K., Shiozaki, K., Ueda, M. & Sato, M. Symmetry and topology in non-Hermitian physics. *Phys. Rev. X* **9**, 041015 (2019).
- Zhou, H. & Lee, J. Y. Periodic table for topological bands with non-Hermitian symmetries. *Phys. Rev. B* **99**, 235112 (2019).
- Rudner, M. S. & Levitov, L. S. Topological transition in a non-Hermitian quantum walk. *Phys. Rev. Lett.* **102**, 065703 (2009).
- Esaki, K., Sato, M., Hasebe, K. & Kohmoto, M. Edge states and topological phases in non-Hermitian systems. *Phys. Rev. B* **84**, 205128 (2011).
- Zhu, B., Lü, R. & Chen, S. PT symmetry in the non-Hermitian Su–Schrieffer–Heeger model with complex boundary potentials. *Phys. Rev. A* **89**, 062102 (2014).
- Rudner, M. S., Lindner, N. H., Berg, E. & Levin, M. Anomalous edge states and the bulk–edge correspondence for periodically driven two-dimensional systems. *Phys. Rev. X* **3**, 031005 (2013).
- Asbóth, J. K. & Obuse, H. Bulk–boundary correspondence for chiral symmetric quantum walks. *Phys. Rev. B* **88**, 121406(R) (2013).
- Deng, T. & Yi, W. Non-Bloch topological invariants in a non-Hermitian domain-wall system. *Phys. Rev. B* **100**, 035102 (2019).
- Yao, S., Yan, Z. & Wang, Z. Topological invariants of Floquet systems: general formulation, special properties, and Floquet topological defects. *Phys. Rev. B* **96**, 195303 (2017).
- Fruchart, M. Complex classes of periodically driven topological lattice systems. *Phys. Rev. B* **93**, 115429 (2016).
- Longhi, S. Non-Bloch PT symmetry breaking in non-Hermitian photonics quantum walks. *Opt. Lett.* **44**, 5804–5807 (2019).
- Helbig, T. et al. Observation of bulk boundary correspondence breakdown in topoelectrical circuits. Preprint at <https://arxiv.org/abs/1907.11562> (2019).
- Ghatak, A., Brandenbourger, M., van Wezel, J. & Coullais, C. Observation of non-Hermitian topology and its bulk–edge correspondence. Preprint at <https://arxiv.org/abs/1907.11619> (2019).

Publisher's note Springer Nature remains neutral with regard to jurisdictional claims in published maps and institutional affiliations.

© The Author(s), under exclusive licence to Springer Nature Limited 2020

Methods

Experimental implementation. As illustrated in Fig. 2, the walker photon is initialized in the spatial mode $x = -1$ and projected onto one of the polarization states $|\pm\rangle$, $|0\rangle$ or $|1\rangle$ via a PBS and a HWP labelled 'H₀'. The coin operator R is implemented by a set of HWPs. The shift operator S_1 (S_2) is implemented by a beam displacer whose optical axis is cut so that the vertically polarized photons are directly transmitted and those with horizontal polarization undergo a lateral displacement into a neighbouring mode. The mode-selective loss operator M_E is implemented by a PPBS. At each step, after applying M_E , photons in the state $|1\rangle$ are reflected by the PPBS with probability p , and the rest continue propagating in the quantum-walk dynamics. The photon is detected by APDs in the modules M_\pm in coincidence with the trigger photon. Details of these detection modules are given in the Supplementary Information. Photon counts give measured probabilities after correcting for relative efficiencies of the different APDs.

Non-Bloch topological invariants. Bloch topological invariants of the quantum-walk dynamics are calculated through the Fourier component $U(k)$ of U in equation (1). We first define two branches of effective Hamiltonians through $H_{\text{eff}}^\epsilon(k) = i\ln_\epsilon U(k)$, where $\epsilon = 0, \pi$ indicates the location of the branch cut. It follows that the imaginary part of the function $\ln_\epsilon U(k)$ belongs to the range $[\epsilon - 2\pi, \epsilon]$. We then invoke periodized time-evolution operators^{40,43,44} to generate topological invariants. For our chiral-symmetric case, we need only its half-period value^{43,44}, defined as

$$\bar{U}_\epsilon(k) = U_{\frac{1}{2}}(k)e^{iH_{\text{eff}}^\epsilon}, \quad (6)$$

where the half-period operator $U_{\frac{1}{2}}(k)$ is the Fourier component of $U_{\frac{1}{2}} := M^{\frac{1}{2}}R(\frac{\theta_2}{2})S_1R(\frac{\theta_1}{2})$, with $M^{\frac{1}{2}} = \begin{pmatrix} e^{\frac{i\epsilon}{2}} & 0 \\ 0 & e^{-\frac{i\epsilon}{2}} \end{pmatrix}$. The Bloch winding numbers are given by equation (3) in the main text, where the integration is over the Brillouin zone with $k \in [0, 2\pi)$.

To calculate the non-Bloch topological invariants, it is necessary to generalize the Brillouin zone to the complex plane using information from the now localized bulk states. Following the framework outlined in the main text, we replace the standard Bloch phase factor e^{ik} by $\beta_{\alpha,j} = |\beta_{\alpha,j}(p_j^\alpha)|e^{i\theta_j^\alpha}$, whose trajectory forms the j th generalized Brillouin zone of the corresponding bulk. In practice, we need to make the substitution $k \rightarrow p_j^\alpha - i\ln|\beta_{\alpha,j}(p_j^\alpha)|$ in equation (3) and integrate over the corresponding generalized Brillouin zone. Note that for the domain-wall system here, two generalized Brillouin zones exist for each given bulk, both yielding the same non-Bloch winding numbers. Details of the calculation of $\beta_{\alpha,j}$ are given in the Supplementary Information.

Finally, we checked that topological invariants calculated via periodized Floquet operators are the same as those defined with Floquet operators in different time frames⁴¹, provided that the generalized Brillouin zones are used. As we detail in the Supplementary Information, by defining a shifted Floquet operator

$$U' = M^{\frac{1}{2}}R(\frac{\theta_2}{2})S_1R(\theta_1)S_2R(\frac{\theta_2}{2})M^{\frac{1}{2}}, \quad (7)$$

and calculating its winding number $\tilde{\nu}'$ over the generalized Brillouin zone, we have

$$\tilde{\nu}'_{0(x)} = \frac{\tilde{\nu} \pm \tilde{\nu}'}{2}. \quad (8)$$

Here, $\tilde{\nu}$ is the winding number of U calculated over the generalized Brillouin zone.

Detection scheme for edge states with the non-Hermitian skin effect. In previous experiments of topological quantum-walk dynamics, topological edge states were detected by observing the localization of the probability distribution near the boundary at long times. However, this method fails in our system because both the edge and bulk states are localized. To unambiguously detect edge states in quantum-walk dynamics, we developed a detection scheme based on the fact that the quasi-energy of edge states is either $\epsilon = 0$ or $\epsilon = \pi$, dictated by chiral symmetry. Our scheme relies on reconstructing time-evolved states at each time step. A weighted summation of wave functions at all time steps then selectively retains the contribution of edge states with either $\epsilon = 0$ or $\epsilon = \pi$, as contributions from all other states cancel out due to interference.

More concretely, the time-dependent wave function can be written as

$$|\Phi(t)\rangle = U^t|\Phi(0)\rangle = \sum_n e^{-iE_n t} \Phi_n |\psi_n\rangle, \quad (9)$$

where E_n is the quasi-energy spectrum, $\Phi_n = \langle \chi_n | \Phi(0) \rangle$, $U|\psi_n\rangle = e^{-iE_n} |\psi_n\rangle$ and $\langle \chi_n | U^{-1} = \langle \chi_n | e^{iE_n}$. By definition, $|\psi_n\rangle$ ($\langle \chi_n |$) is the right (left) eigenvector of U (ref. 48).

Substituting equation (9) into equation (4), for large t , we have

$$|\Phi_\epsilon(t)\rangle = \sum_n f_\epsilon(E_n) \Phi_n |\psi_n\rangle, \quad (10)$$

where

$$f_\epsilon(E_n) = \begin{cases} \frac{1}{t+1} \frac{1 - \exp[-i(E_n - \epsilon)(t+1)]}{1 - \exp[i(E_n - \epsilon)]} & E_n \neq \epsilon \\ 1 & E_n = \epsilon \end{cases}, \quad (11)$$

with $\epsilon = 0, \pi$.

When E_n is completely real, $\lim_{t \rightarrow \infty} f_\epsilon(E_n) \rightarrow 0$ for $E_n \neq \epsilon$. Signals only from topological edge states would remain in the long-time dynamics, provided that the corresponding coefficient Φ_n is non-vanishing, that is, the initial state has a finite overlap with the left eigenvector of the relevant edge state.

Experimentally, we probed the projection of the wave-function summations $\Phi_{\epsilon,\mu}(x) = |\langle \chi | \otimes \langle \mu | \Phi_\epsilon(t) \rangle|$ such that the internal and external degrees of freedom of both types of topological edge states ($\epsilon = 0, \pi$) are fully resolved.

Experimental implementation of edge-state detection. We probed $\Phi_{\epsilon,\mu}(x)$ from our experimental reconstruction of $|\varphi(t)\rangle$ at each time step. Here, $|\varphi(t)\rangle$ is the experimentally realized time-dependent state (with M_E rather than M), which is related to $|\Phi(t)\rangle$ through $|\varphi(t)\rangle = e^{-\gamma t} |\Phi(t)\rangle$. It follows that

$$\Phi_{\epsilon,\mu}(x) = \left| \langle \chi | \otimes \langle \mu | \sum_{t'=0}^t \frac{e^{i\epsilon t'}}{t+1} e^{\gamma t'} |\varphi(t')\rangle \right|. \quad (12)$$

Since U and initial states are purely real in the basis of $\{|\pm\rangle\}$, we have the expansion

$$|\varphi(t)\rangle = \sum_x [p_+(t,x)|x\rangle \otimes |+\rangle + p_-(t,x)|x\rangle \otimes |-\rangle], \quad (13)$$

where the coefficients $p_\pm(t,x)$ are also real. Based on these, we performed four distinct measurements with detection modules M_i (where $i = 1, \dots, 4$) to reconstruct $|\varphi(t)\rangle$ in the basis $\{|\pm\rangle\}$. This amounts to measuring the absolute values, the relative signs and a global sign of the real coefficients $\{p_\pm(t,x)\}$, as we detail in the following. All measurement modules are shown in Fig. 2.

First, we measured the absolute values $|p_\pm(t,x)|$. After the t th step, photons in the spatial mode x were sent to detection module M_1 , consisting of a HWP (H_1) at 22.5° , a PBS and APDs. Detection module M_1 applied a projective measurement of the observable σ_x on the polarization of photons. The counts of the horizontally polarized photons, $N_H(t,x)$, and vertically polarized ones, $N_V(t,x)$, were registered by the coincidences between one of the APDs in the detection module and the APD for the trigger photon. The measured probability distributions are $P_{H(V)}(t,x) = N_{H(V)}(t,x) / \sum_x [N_H(t,x) + N_V(t,x) + \sum_{t'=0}^t N_L(t',x)]$, with $N_L(t,x)$ the photon loss caused by the partial measurement M_E . The square root of the probability distribution $P_{H(V)}(t,x)$ corresponds to $|p_\pm(t,x)|$.

Second, we determined the relative sign between the amplitudes $p_+(t,x)$ and $p_-(t,x)$ via detection module M_2 . The only difference between modules M_2 and M_1 is that the setting angle of the HWP (H_1) is 0 , that is, a projective measurement of the observable σ_z on the polarization of photons. The difference between the probability distributions of the horizontally and vertically polarized photons is given by

$$P_H(t,x) - P_V(t,x) = 2p_+(t,x)p_-(t,x), \quad (14)$$

which determines the relative sign between $p_+(t,x)$ and $p_-(t,x)$.

Third, we probed the relative sign between $p_\pm(t,x)$ and $p_\pm(t,x-1)$, which is required to calculate the summation of wave functions at each time step. To this end, we added a third detection module, M_3 , behind modules M_1 and M_2 (Fig. 2), consisting of two HWPs (H_2 and H_3) at 22.5° , a beam displacer, a PBS and APDs. We used a beam displacer to combine the horizontally polarized photons in the spatial mode x and the vertically polarized photons in the spatial mode $x-1$. After a projective measurement on the polarizations of photons via HWP H_3 and the next PBS, the difference in the probability distribution of the resulting photons between the two polarizations is

$$P_H(t,x) - P_V(t,x) = p_+(t,x)p_+(t,x-1) \quad (15)$$

when HWP H_1 is set at 22.5° in modules M_1 and M_2 , and

$$P_H(t,x) - P_V(t,x) = p_-(t,x)p_-(t,x-1) \quad (16)$$

when the setting angle of HWP H_1 is -22.5° . Note that detection module M_3 measures the relative sign between $p_\pm(t,x)$ and $p_\pm(t,x-1)$ for arbitrary values of x .

Finally, we determined the global sign of $p_\pm(t,x)$ relative to the reference photons, which are reflected by the PBS used for the preparation of the initial coin state. For this step, we needed to determine the sign only of $p_\pm(t,x_w)$ for an arbitrary position x_w at each time step. A natural choice of x_w is the position where the walker and reference photons have comparable counts. Assuming that the reference photons have an amplitude a (where $a > 0$), we determined the relative sign between the amplitudes of the reference photons and the walker photons at x_w after t steps. We removed detection module M_3 and kept the optical elements of modules M_1 and M_2 . Only photons reflected by the PBS in modules M_1 and M_2 are relevant here. These photons, after passing through HWP H_4 at 45° , are combined with the reference photons at a PBS. A projective measurement is then applied on the polarization of the photons via HWP H_5 at 22.5° and the last PBS. The difference between the probabilities of the photons with different polarizations is

$$P_H(t,x_w) - P_V(t,x_w) = 2ap_-(t,x_w), \quad (17)$$

which determines the global sign of $p_{\pm}(t, x_w)$ as a is positive. Since we have determined the relative sign between $p_{+}(t, x)$ and $p_{-}(t, x)$ via M_2 and that between $p_{\pm}(t, x)$ and $p_{\pm}(t, x-1)$ via M_3 , the global sign of $p_{\pm}(t, x)$ is also determined for an arbitrary value of x .

With the above steps, we reconstruct $|\varphi(t)\rangle$ in the basis of $|\pm\rangle$, which enables us to calculate $\Phi_{\pm\theta}(x)$ according to equation (12).

Data availability

The data represented in Figs. 3–5 are available as Source Data. All other data that support the plots within this paper and other findings of this study are available from the corresponding authors upon reasonable request.

References

48. Brody, D. C. Biorthogonal quantum mechanics. *J. Phys. A Math. Theor.* **47**, 035305 (2014).

Acknowledgements

This work has been supported by the National Natural Science Foundation of China (grant nos. 11674056, 11674189, U1930402 and 11974331) and a start-up fund from the Beijing Computational Science Research Center. W.Y. acknowledges support

from the National Key Research and Development Program of China (grant nos. 2016YFA0301700 and 2017YFA0304100).

Author contributions

L.X. performed the experiments, with contributions from K.W. and G.Z.; W.Y., T.D. and Z.W. developed the theoretical aspects and performed the theoretical analysis; P.X. designed the experiments and analysed the results; P.X., W.Y. and Z.W. wrote the paper, with input from all authors.

Competing interests

The authors declare no competing interests.

Additional information

Supplementary information is available for this paper at <https://doi.org/10.1038/s41567-020-0836-6>.

Correspondence and requests for materials should be addressed to Z.W., W.Y. or P.X.

Peer review information *Nature Physics* thanks Andrea Alu and the other, anonymous, reviewer(s) for their contribution to the peer review of this work.

Reprints and permissions information is available at www.nature.com/reprints.